Melt supply variations to a magma-poor ultra-slow spreading ridge (Southwest Indian Ridge 61° to 69°E)

Mathilde Cannat, Céline A Rommevaux-Jestin, Hiromi Fujimoto

Geochemistry Geophysics Geosystems G3
AN ELECTRONIC JOURNAL OF THE EARTH SCIENCES
Published by AGU and the Geochemical Society

Article
Volume 4, Number 8
1 August 2003
9104, doi:10.1029/2002GC000480
ISSN: 1525-2027

Melt supply variations to a magma-poor ultra-slow spreading ridge (Southwest Indian Ridge 61° to 69°E)

Mathilde Cannat and Céline Rommevaux-Jestin
Laboratoire de Géosciences Marines/CNRS, UMR 7097, IPGP/Université Pierre et Marie Curie, 4 place Jussieu, 75252 Paris Cedex 05, France (cannat@ipgp.jussieu.fr; rommevau@ipgp.jussieu.fr)

Hiromi Fujimoto
Research Center for the Prediction of Earthquakes and Volcanic Eruptions, Tohoku University, Aoba-ku, Sendai, 980-8578, Japan (fujimoto@aob.geophys.tohoku.ac.jp)

[1] The Southwest Indian Ridge (SWIR) to the east of the Melville Fracture zone receives anomalously low volumes of melt on average. However, a small number of ridge segments appear to receive more melt than this regional average. We use off-axis bathymetry, gravity, and magnetic data to show that this melt distribution pattern, quite distinct from what is observed at the Mid-Atlantic Ridge (MAR), has been a characteristic of the easternmost SWIR for at least the past 10 myr. We also show that segments of the easternmost SWIR are substantially shorter lived than most segments of the MAR. Melt distribution in our SWIR study area is therefore both more focused and more variable in time than at the MAR. We tentatively propose a mechanism by which strong and transient melt-focusing events could be initiated by a localized increase in the volume of melt supplied by the melting mantle to the base of the axial lithosphere, causing thermal thinning of this lithosphere and along-axis melt migration. These two processes may combine to effectively focus larger volumes of melt toward the center of future thick crust segments. Rapid melt extraction by dikes that feed large volcanic constructions on the seafloor, followed by tectonic disruption of these volcanic constructions by deep-reaching faults, may then cool the axial lithosphere back to its original thickness and end the melt-focusing events. The easternmost SWIR is also characterized by a common departure from isostatic compensation of seafloor topography and by a pronounced asymmetry of crustal thickness and seafloor relief between the two ridge flanks. At the faster spreading MAR, similar characteristics are found near the ends of ridge segments. We propose that spreading at the ultra-slow SWIR during periods when the melt supply is low (i.e., most of the time for the easternmost SWIR) is dominated by large offset asymmetric normal faulting, with significant flexural uplift of the footwalls. Faults face either north or south, and changes in fault polarity are frequent, both along axis and along flow lines (i.e., with time). Producing large faults and maintaining high uncompensated reliefs require the axial lithosphere to be thick, a predictable characteristic for this ultra-slow ridge, which has an anomalously low regionally averaged melt supply.

Components: 6912 words, 14 figures, 1 table.

Keywords: mid-ocean ridge; slow spreading rate; melt supply; crustal thickness; extensional faulting.

Index Terms: 3035 Marine Geology and Geophysics: Mid-ocean ridge processes; 3010 Marine Geology and Geophysics: Gravity; 8122 Tectonophysics: Dynamics, gravity and tectonics; 8434 Volcanology: Magma migration; 8010 Structural Geology: Fractures and faults.

Received 25 November 2002; **Revised** 20 May 2003; **Accepted** 27 May 2003; **Published** 1 August 2003.

Cannat, M., C. Rommevaux-Jestin, and H. Fujimoto, Melt supply variations to a magma-poor ultra-slow spreading ridge (Southwest Indian Ridge 61° to 69°E), *Geochem. Geophys. Geosyst.*, *4*(8), 9104, doi:10.1029/2002GC000480, 2003.

Theme: Accretionary Processes Along the Ultra-Slow Spreading Southwest Indian Ridge
Guest Editors: Catherine Mevel and Daniel Sauter

1. Introduction

[2] Regional axial depths along the ultra-slow (~15 mm/yr full-rate [*Patriat and Segoufin*, 1988]) Southwest Indian Ridge (SWIR) vary from an average of 3100 m between 49°E and the Gallieni FZ, to 4700 m between the Melville Fracture Zone and the Rodrigues Triple Junction (RTJ). This range of axial depths is consistent with variations of average crustal thickness from a little more than 6 km between 49°E and the Gallieni FZ, to a little less than 3 km between the Melville Fracture Zone and the RTJ (assuming isostatic compensation of the ridge topography at the regional scale, a compensation depth of 200 km, and a reference depth of 3500 m for a crustal thickness of 5.5 km [*Cannat et al.*, 1999]). Seismic data are available for a 100 km-long near-axis profile in the Melville to RTJ region, yielding an average crustal thickness of 3.7 km (location in Figure 6a [*Muller et al.*, 1999]). Regional axial depths and seismic data therefore concur in indicating anomalously thin crust in this easternmost part of the SWIR. Serpentinized peridotites make a significant proportion of the rocks dredged along axis in this region [*Mével et al.*, 1997; *Seyler et al.*, 2003], crustal thicknesses there thus give us a maximum estimate for the amount of melt provided to the crust per unit length of plate separation.

[3] The SWIR east of the Melville FZ also displays anomalous axial morphologies and gravity signatures [*Cannat et al.*, 1999; *Mendel et al.*, 1997; *Rommevaux-Jestin et al.*, 1997]. Three segments (#8, 11 and 14; Figure 1) have an along-axis relief >2000 m and moderate to large ΔMBA (the MBA variation between segment center and segment ends). The other segments have small along-axis relief, and small to zero ΔMBA. In comparison, other regions of the SWIR, and most regions of the faster spreading Mid-Atlantic Ridge (MAR), show a more regular segmentation pattern, with moderate axial reliefs and ΔMBA. Seafloor morphology [*Cannat et al.*, 1999; *Mendel et al.*, 1997], seafloor reflectivity [*Parson et al.*, 1997], and submersible studies [*Fujimoto et al.*, 1999] show that high relief segments of the Melville to RTJ region correspond to large volcanic constructions, that fill the axial valley at segment centers. These volcanic constructions are significantly larger than the axial volcanic ridges (AVRs) that have been described in many MAR segments [*Smith and Cann*, 1999], but could be similar to volcanic features described at the ultra-slow Gakkel and Knipovitch Ridges, in the Arctic [*Dick et al.*, 2001; *Kurras et al.*, 2001; *Okino et al.*, 2002; *Cochran et al.*, 2003].

[4] Seismic crustal thickness data acquired along the 100 km-long CAM116 profile [*Muller et al.*, 1999] show that, in addition to having a reduced average crustal thickness, the easternmost SWIR shows significant variations in the average crustal thickness of individual ridge segments, some segments having average crustal thickness values larger than the regional average (high relief segment #8 and paleo-segment #6′; Table 1). By contrast, average seismic crustal thicknesses determined for various segments of the MAR are more consistent [*Hooft et al.*, 2000; *Tolstoy et al.*, 1993; *Wolfe et al.*, 1995]. This is illustrated in Table 1 for three MAR segments in the 35°N region [*Hooft et al.*, 2000]. Seismic data for other MAR segments confirm this tendency. Assuming that seismic crustal thicknesses are, if not equivalent, at least closely related to the ridge's melt supply, the comparison of the SWIR and MAR seismic data sets therefore suggests that there is a fundamental difference in the way melt is distributed along axis in the two regions: along the MAR, ridge segments appear to be supplied with the regional average amount of melt; along the Melville to RTJ region of the SWIR, some segments appear

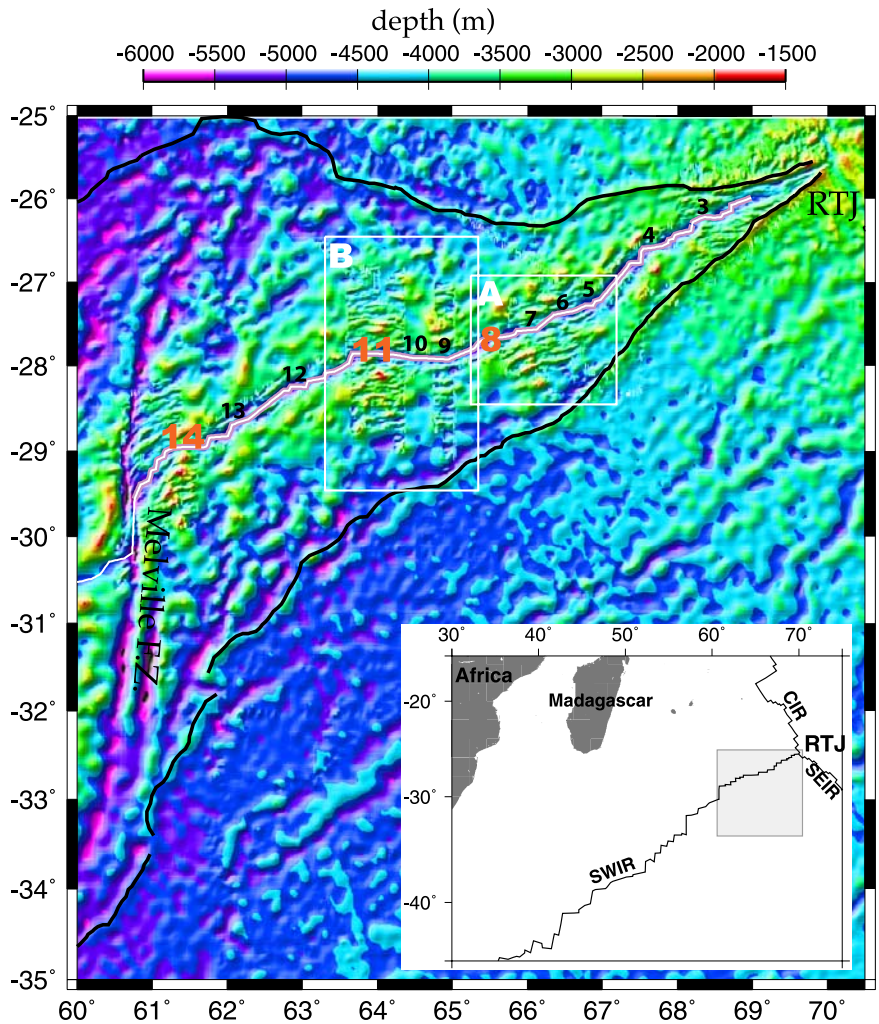

Figure 1. Topographic map of the Southwest Indian Ridge (SWIR) between 60°E and 70°E, from shipboard bathymetric data and satellite-derived bathymetry [*Smith and Sandwell*, 1997]. RTJ: Rodrigues triple Junction; CIR: central Indian Ridge; SEIR: Southeast Indian Ridge. A: location of Figure 6. B: location of Figure 9. Ridge segments 8, 11 and 14 (in red) have high along-axis reliefs; other ridge segments (in black) have low along axis relief.

to receive more melt than the regional average, while the intervening ridge segments appear to receive less.

[5] In this paper, we investigate topographic and crustal thickness variations in space and time, using off-axis bathymetry, gravity, and magnetic data acquired during the Rodrigues cruise in the 66°E region (Box A in Figure 1 [*Schlich et al.*, 1987]), and during the INDOYO cruise in the 64°E region (Box B in Figure 1 [*Fujimoto et al.*, 1999]). This leads us to address the question of the spatial and temporal variability of melt distribution in the Melville to RTJ region of the SWIR, and to discuss

Table 1. Comparison of Mean Seismic Crustal Thicknesses Determined Between 65°30′E and 66°30′E on the SWIR and Between 33°N and 35°N on the Mid-Atlantic Ridge

SWIR[a]	MAR[b]
Segment 8: 4.7 km	segment OH1: 5.6 km
Paleo-segment 7: 2.9 km	segment OH2: 5.7 km
Paleo-segment 6′: 4.1km	segment OH3: 5.1 km
Average CAM116	OH1-OH2-OH3
(100 km): 3.7 km	(200 km): 5.5 km

[a] CAM116 profile [*Muller et al.*, 1999]; see location in Figure 6a.
[b] Ridge segments OH1, OH2, and OH3 [*Hooft et al.*, 2000].

its effects on the crustal architecture of this ultra-slow ridge.

2. Data Acquisition and Processing

[6] Multibeam bathymetry, gravity and magnetism data for the 66°E region [*Mendel et al.*, 1997; *Munschy*, 1987; *Schlich et al.*, 1987] were acquired in 1984 on board the RV Jean Charcot (Rodrigues II cruise) along north-south, flow line parallel profiles spaced by ~3 km. Transit Satellite navigation system was used during this cruise, but comparison of the SeaBeam swaths at crossing points indicates an accuracy of about 300 m for the navigation of these profiles [*Munschy and Schlich*, 1989]. Later acquisition of a few crosscutting Simrad swaths in the same area (Capsing cruise on board R/V L'Atalante, 1993) improved the position accuracy to about 120 m [*Mendel et al.*, 1997]. Mean accuracy of bathymetry data is about 70 m for Seabeam and 50 m for SIMRAD. Gravity data were acquired during the two cruises with the same Bodenseewerk KSS-30 marine gravity meter, with an accuracy of 3 to 4 mGal [*Rommevaux-Jestin et al.*, 1997; *Schlich et al.*, 1987]. Magnetic data were acquired using a proton magnetometer Geometrics 801 during the Rodrigues II cruise, with a precision of about 6 nT [*Schlich et al.*, 1987].

[7] Data for the 64°E region were acquired on board the RV Yokosuka in 1998 (Indoyo Cruise), along north-south, flow line parallel profiles spaced by ~8 km. Multibeam bathymetry was acquired using the Furuno HS-10 system which comprises 45 beams, operating at 12 kHz. Data accuracy is about 25 m. Magnetic data were acquired using a STC 10 towed proton magnetometer (data accuracy ~2 nT), and gravity data using a LaCoste & Romberg S-63 sea gravimeter (data accuracy ~2 mGal).

2.1. Processing of Magnetic Data

[8] Magnetic data were corrected for the International Geomagnetic Reference Field [*International Association of Geomagnetism and Aeronomy et al.*, 2000] to obtain magnetic anomalies. We then compared magnetic anomalies measured along flow line-parallel profiles, with synthetic magnetic anomaly profiles, and identified a sequence of magnetic anomalies starting with the central anomaly and including anomalies 2, 2A, 3, 3A and 5 (Figure 2). The synthetic magnetic anomaly profile was generated with a two-dimensional block model incorporating the calibrated magnetic inversion timescale of *Cande and Kent* [1995], as shown in Figure 2. Our picks correspond to finite spreading rates of 13.5–14 mm/yr since the time of magnetic anomaly 5, and ~15 mm/yr since the time of magnetic anomaly 2A. These rates are within the range proposed by *Patriat and Segoufin* [1988]. Fits are also reasonably good in most cases using *Patriat and Segoufin* [1988] rotation poles.

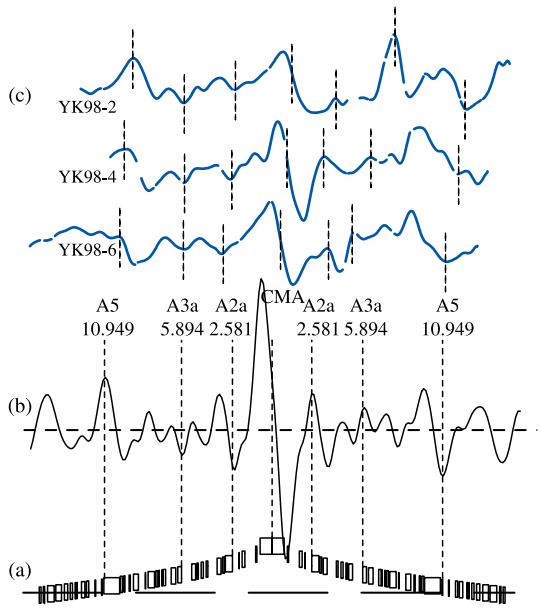

Figure 2. Example of magnetic anomaly picking. From bottom to top: (a) two-dimensional block model incorporating the calibrated magnetic inversion timescale of *Cande and Kent* [1995], with a half spreading rate of 7 mm/yr, and a magnetic layer thickness of 400 m; (b) synthetic magnetic anomaly profile calculated from this block model at 28°S, 64°E, with a north-south spreading direction, and 0.7 km-wide transitions between blocks of opposite polarities; (c) Magnetic anomaly profiles YK98-2, YK98-4 and YK98-6, measured during the Indoyo cruise in the 64°E area. Magnetic anomalies (central magnetic anomaly or CMA, Anomaly 2a, 3a and 5) are picked as indicated by dashed lines on both synthetic and measured magnetic anomaly profiles.

2.2. Processing of Gravimetry Data

[9] The effect of a constant thickness (3 km), constant density (2700 kg/m3) crust was removed

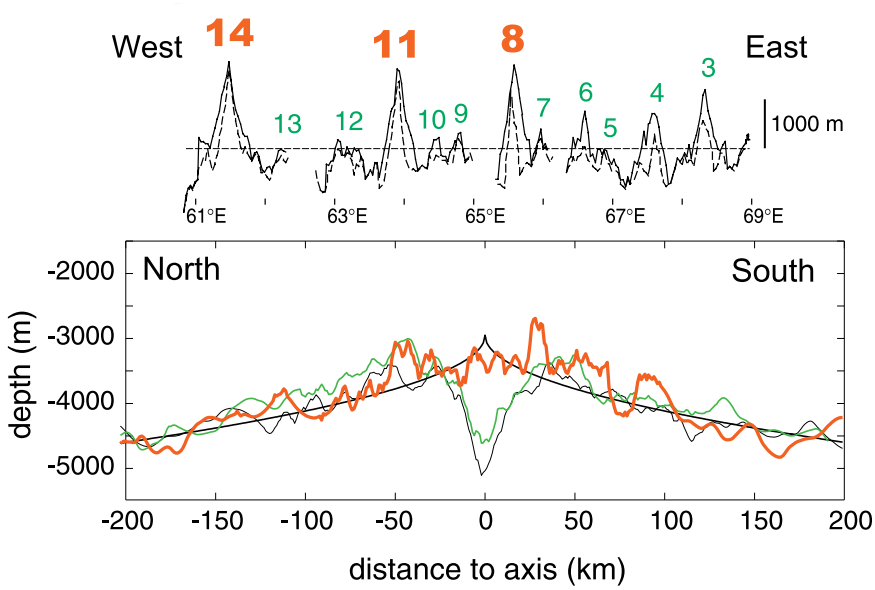

Figure 3. Upper panel: along-axis bathymetric profile for the SWIR between 61°E and 69°E (dashed line: maximum depth of axial valley). Bottom panel: average across-axis bathymetric profiles at center of high relief segments (average of 3 profiles, in red), at center of low relief segments (average of 9 profiles, in green), and at segment ends (average of 14 profiles, in gray). Individual bathymetric profiles use shipboard bathymetry when available, and satellite-derived bathymetry elsewhere (see Figure 1). Subsidence curve follows the empirical depth (Z) versus age (t) curve of *Parsons and Sclater* [1977]: ($Z(t) = Ct^{1/2} + Z_0$), assuming symmetrical spreading about the present-day axis, with $Z_0 = -3000$ m and $C = -340$ m/myr$^{1/2}$.

from Free Air Anomaly data to obtain Mantle Bouguer Anomaly (MBA) values. Satellite-derived topography [*Smith and Sandwell*, 1997] was used in MBA calculations to fill up gaps in the shipboard bathymetry record, and to avoid corner effects. Only areas with shipboard bathymetric coverage are considered in the interpretation of gravimetric data. The effect of cooling of the plates with age was calculated as a function of distance to the ridge axis, using the poles and rates of plate motion published for the 64°E region [*Patriat and Segoufin*, 1988]. The subsidence rate was chosen so as to provide the best fit with across-axis bathymetric profiles drawn at the center and ends of the 12 segments identified in the study area (Figure 3). The gravity effect of cooling of the plates with age was removed from the MBA to obtain residual MBA (RMBA) values. We then inverted these residual anomalies for crustal thickness following the method of *Kuo and Forsyth* [1988]. This method assumes that gravity anomalies only reflect crustal thickness variations. It involves a downward continuation of RMBA to a constant depth below sea level (here 7 km), corresponding to the inferred average Moho depth. To avoid instabilities inherent to downward continuation of short wavelengths anomalies, a filter is applied which cosine tapers the RMBA signal with wavelengths between 35 and 25 km, and cuts off the RMBA signal with wavelengths <25 km (corresponding to sources located at depths less than the downward continuation depth).

[10] The best fit between gravity-derived crustal thickness estimates and seismic crustal thicknesses determined along the CAM116 profile [*Muller et al.*, 1999] was obtained for gravity models calculated with a reference crustal thickness of 3 km, and a downward continuation depth of 7 km (a water depth of 4 km and 3 km of crust; Figure 4). Gravity-derived crustal thickness estimates in Figure 4 are very similar to seismic crustal thickness values in thick crust portions of the profile, and the amplitude of lateral crustal thickness variations is similar. However, in the thin crust area that corresponds to paleo-segment 7 (Figure 4), gravity-derived estimates underestimate the actual (seismic) crustal thickness. This indicates that the gravity model's

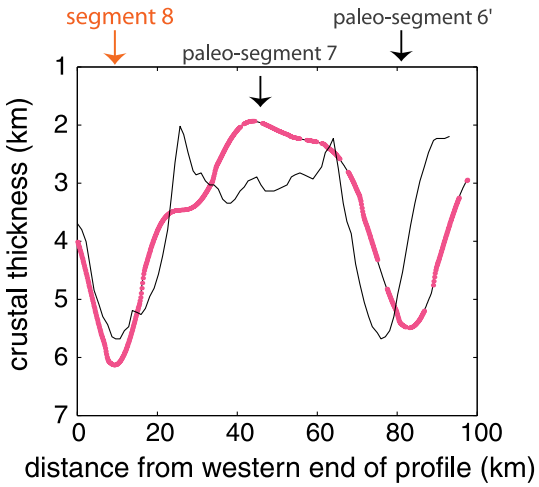

Figure 4. Crustal thickness modeled using gravity data (this study) (in red), compared with crustal thickness determined from seismic data [*Muller et al.*, 1999] (in gray), along profile CAM116 (see location in Figure 6a).

assumptions of constant crustal and mantle densities are not valid in this part of the profile. The seismic velocity structure determined by *Muller et al.* [1999] for the CAM116 profile shows that, as also observed in along-axis seismic records from the MAR [*Canales et al.*, 2000; *Detrick et al.*, 1993; *Tolstoy et al.*, 1993], the thin crust area has near normal layer 2 thickness, while layer 3 is thin or absent. This suggests that the overall density of the crust is less there than in thicker crust portions of the profile. Crust modeled from gravity using the constant crustal density assumption should therefore be thicker, and not thinner than the seismic crust, in this thin crust area. The difference between gravity-derived crustal thickness and seismic crustal thickness beneath paleo-segment 7 is thus probably due to lateral changes in the density of the upper mantle: denser (colder, less melt-impregnated, or less serpentinized) mantle beneath thin crust, lighter (hotter, more melt-impregnated, or more serpentinized) mantle beneath thicker crust. The seismic velocity models published by *Muller et al.* [1999] do not reach into the mantle and therefore do not allow to test this hypothesis.

[11] In order to qualitatively assess the degree of compensation of seafloor topography, we have compared gravity-derived crustal thicknesses, with crustal thicknesses calculated for the case of perfect Airy compensation of seafloor relief, using constant crust, mantle and water densities (2700 kg/m3, 3300 kg/m3 and 1000 kg/m3). Airy crustal thickness values depend strongly on the choice of a reference seafloor depth and crustal thickness, and should therefore be used with this limitation in mind. For off-axis regions (i.e., outside the axial valley), we made the hypothesis that topography predicted using the *Parsons and Sclater* [1977] relationship would be compensated by the reference 3 km-thick crust used in our RMBA inversion. For on-axis regions (i.e., within the axial valley), where *Parsons and Sclater* [1977] predicted topography is clearly wrong, we made the hypothesis that seafloor lying at the mean axial depth would be compensated by the mean gravity-derived axial crustal thickness.

3. Past Segmentation Patterns in the Melville to RTJ Region

[12] Segment ends in the Melville to RTJ region generally do not coincide with significant offsets of the ridge axis (Figure 1). Instead, they correspond with spreading perpendicular or oblique depressions, while segment centers correspond with spreading perpendicular volcanic ridges [*Mendel et al.*, 1997]. Centers of low relief segments are small volcanic ridges, some only 2–3 km long; centers of high relief segments are prominent volcanic ridges that extend up to 60 km along-axis [*Mendel et al.*, 1997].

[13] Only two present-day segment centers have off-axis traces in the bathymetric map of Figure 1: two sub-parallel north to north-northeast trending alignment of highs, with an intervening alignment of basins, that extend on both flanks of the ridge from the center of segments #13 and 14. The absence of such off-axis alignments to the east of segment #13 suggests that past ridge segmentation patterns there have never lasted long. This conclusion is reinforced by looking at the residual topography in Figure 5: subsidence due to cooling of the plates with age (see Figure 3) has been removed and residual highs and lows to the east of

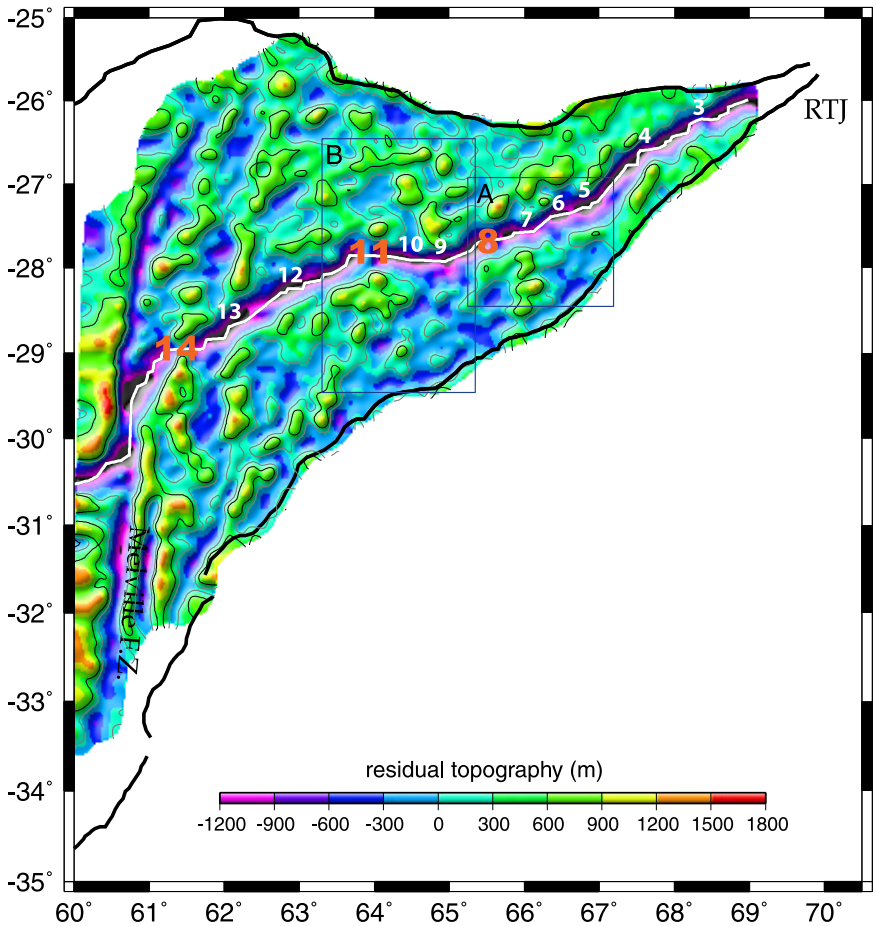

Figure 5. Map of residual topography for the SWIR between 60°E and 70°E. Residual topography is calculated using the bathymetry of Figure 1, subsidence parameters as in Figure 3, and spreading rates and directions published by *Patriat and Segoufin* [1988]: 0 to 11 myr: 16 mm/yr along a N02 direction; 11 to 20 myr: 12 mm/yr along a N183 direction; and 20 to 40 myr: 21 mm/yr along a N06 direction. Contour shows residual topography >500 m. Segment numbers, inset numbers, and acronyms: same as in Figure 1.

segment #13 appear scattered, with no preferred elongation.

4. Topographic and Crustal Thickness Variations in the 66°E Region

[14] Shipboard coverage in the 66°E area extends 15 to 50 km off-axis, over 3 present-day ridge segments: #6, 7, and 8 (Figure 6a). The prominent east-west ridge noted as #6′ in Figure 6 corresponds with a positive RMBA (Figure 6b [*Rommevaux-Jestin et al.*, 1997] and is therefore clearly an uncompensated feature. Gabbros have been dredged on the north flank of this ridge [*Mével et al.*, 1997], that we interpret as a fault bounded block caught between the overlapping ends of segments #6 and 7. This prominent ridge does, however, bear a strong normal magnetic anomaly and could therefore also be the locus of recent volcanism.

[15] Gravity-derived crustal thicknesses ~6 km underlie the center of high relief segment #8, in good agreement with crustal thickness values determined from seismic data (Figure 4). Maximum gravity-derived crustal thicknesses for low relief segments # 6 and 7 are 4 to 5 km (Figures 6c and 7).

[16] Going from west to east in Figure 6b, along the anomaly 2A isochron on the southern ridge flank, one goes from positive RMBA (crust thinner than average), to negative RMBA (crust thicker than average), and back to positive RMBA, each

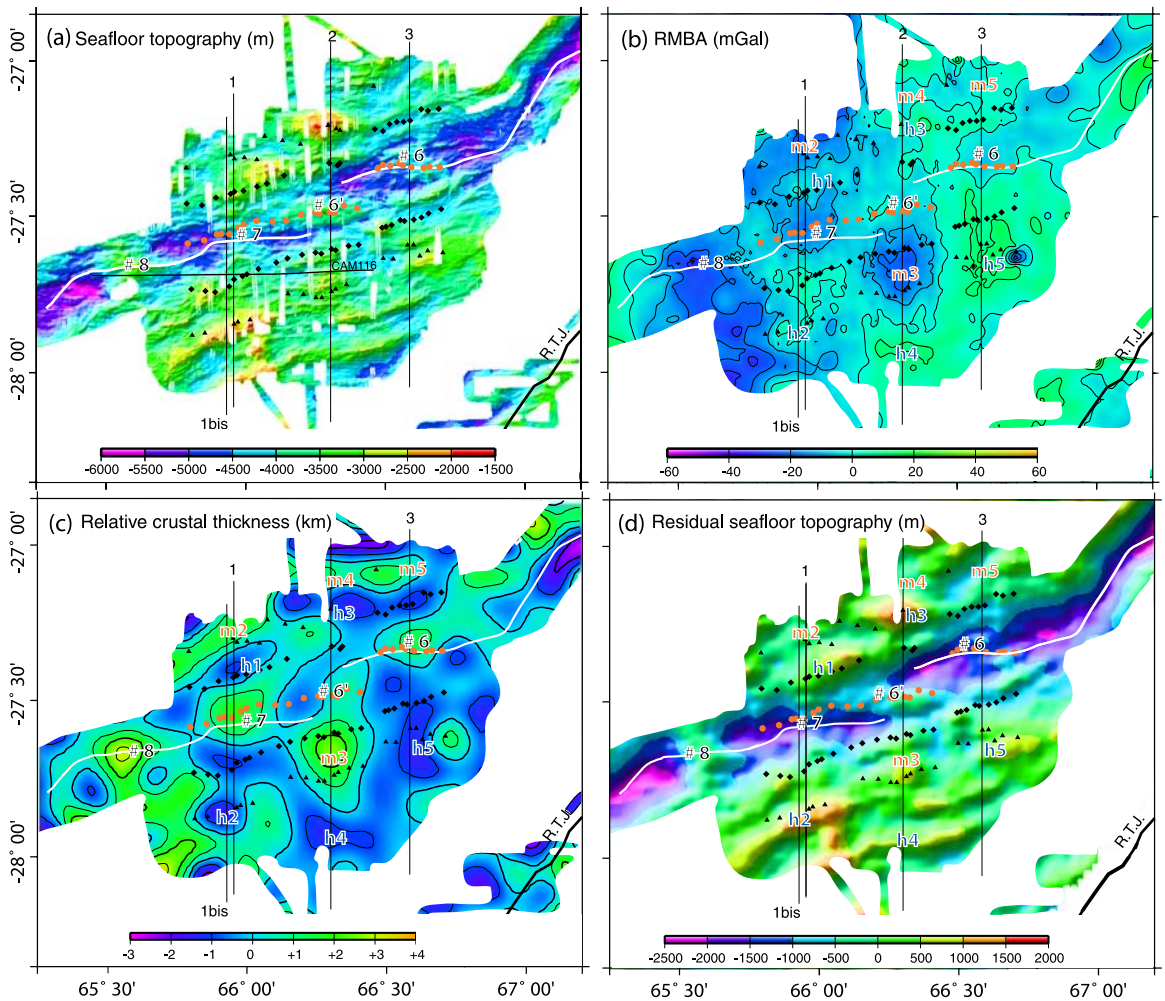

Figure 6. Maps of the 66°E area: (a) detail of Figure 1, showing only shipboard bathymetric data; (b) residual mantle Bouguer Anomaly obtained from shipboard FAA data (see section 2); (c) Relative crustal thickness derived from RMBA map (see section 2); (d) detail of Figure 5, showing only residual topography from shipboard bathymetric data. White line: proposed location of present-day ridge axis ([*Cannat et al.*, 1999]). Red dots: central magnetic anomaly; black losanges: magnetic anomaly 2A; black triangles: magnetic anomaly 3. Thin black lines noted as 1, 1bis, 2, and 3: location of sections shown in Figures 8 and 13. R.T.J.: trace of past locations of the Rodrigues Triple Junction. Letters in red and blue: topographic and gravimetric features discussed in text and also shown in Figures 8 and 13. Letters in red correspond to thicker crust domains; letters in blue correspond to topographic highs that are not associated with thicker than average crust (uncompensated highs).

domain being ~30 km in along-axis width. The negative RMBA domain is on the same flow line as the on axis ridge #6′, that is underlain by thinner than average crust. The eastern domain of positive RMBA (at the time of anomaly 2A) is on the same flow line as present-day segment #6, that is underlain by thicker than average crust.

[17] Across-axis sections (Figure 8) further illustrate this short-scale crustal thickness variability, and the range of crustal thicknesses associated with topographic highs in the area. Section 1, at the longitude of the center of segment #7, cuts through topographic highs noted as h1 and h2 in the residual topography map (Figure 6d), both of which appear to be uncompensated, thin crust features. Topographic high h2 corresponds with our pickings of magnetic anomaly 3 on the southern ridge flank. Crust of similar age on the northern ridge flank, noted as m2 in Figures 6 and 8, appears thicker than average (gravity-derived crustal thickness ~5 km). Along section 2, topo-

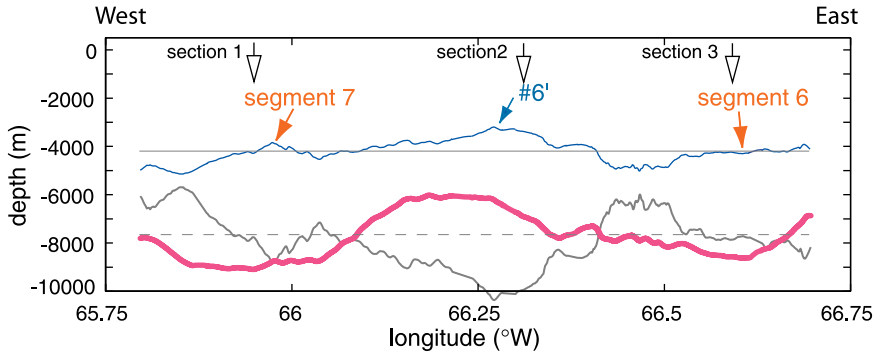

Figure 7. Section along central magnetic anomaly in the 66°E area (see Figure 6). Arrows show intersections with across-axis sections 1, 2, and 3 (see Figure 8). Blue line: actual seafloor topography. Pink line: Moho depth as predicted from gravity data. Thick gray line: Moho topography calculated for the case of perfect Airy compensation of seafloor topography (see Data Processing section). For this calculation, we made the hypothesis that seafloor lying at the mean axial depth in the 66°E area (thin gray line: 4268 m; calculated for axis as defined in Figure 6) would be compensated by the mean gravity-derived axial crustal thickness in the 66°E area (3500 m; also calculated for axis as defined in Figure 6). Thin dashed gray line: reference Moho depth (4268 + 3500 m).

graphic high h3 also corresponds with anomaly 3 on the northern ridge flank, but has thinner than average crust, while a lower-relief region of similar age on the southern ridge flank, noted as m3 in Figures 6 and 8, appears to have thicker than average crust (gravity-derived crustal thickness ~6 km). In crust older than anomaly 3, section 2 cuts through a narrow, uncompensated ridge (h4) on the southern ridge flank, and through a thicker crust domain (m4), on the northern ridge flank. Crustal accretion at the longitude of segment #6 (section 3 in Figure 8) appears similarly asymmetric, with very thin crust underlying topographic high h5 on the southern ridge flank, and thicker crust (gravity-derived crustal thickness ~3.5 km) underlying the topographic low noted as m5, on the northern ridge flank. Topographic high h1 on the northern ridge flank therefore appears exceptional in that crust of equivalent age on the southern ridge flank is similarly thin (Figure 8).

[18] The 66°E area therefore appears characterized by (1) large crustal thickness variations that occur over distances of a few tens of km both along and across-axis, producing a checkerboard pattern in the RMBA map of the area (Figure 6b); (2) a general departure from isostatic compensation of seafloor topography, the highest reliefs (h1, h2, and h3; Figure 6d) being underlain by thinner than average crust; and (3) a pronounced asymmetry of crustal thickness and seafloor relief between the two ridge flanks that switches sense over short distances, both along-axis and along flow lines.

5. Topographic and Crustal Thickness Variations in the 64°E Region

[19] Shipboard coverage in the 64°E region extends 15 to 100 km off-axis, over 3 present-day ridge segments: #9, 10, and 11 (Figure 9a). Seismic crustal thicknesses in the 66°E region are constrained only in the center of segment #11, and beneath its eastern extremity (~6 km and ~3 km, respectively [*Yamada et al.*, 2002]). These seismic crustal thicknesses are in good agreement with our gravity-derived values.

[20] Gravity-derived crustal thicknesses ~6.3 km underlie the center of high relief segment #11, while maximum gravity-derived crustal thicknesses are only 2 to 3 km under the center of low relief segments #9 and 10. These low relief segments actually appear to have thinner crust than neighboring segment ends (Figures 9c and 10).

[21] Coverage off-axis from segments #9 and 11 extends to a bit further than magnetic anomaly 5. The high relief, low RMBA, thick crust center of segment #11 has no off-axis trace; crust formed at this longitude at the time of anomaly 2A has a subdued topography (Figure 9a) and less negative RMBA (Figure 9b). Strongly negative RMBA, and

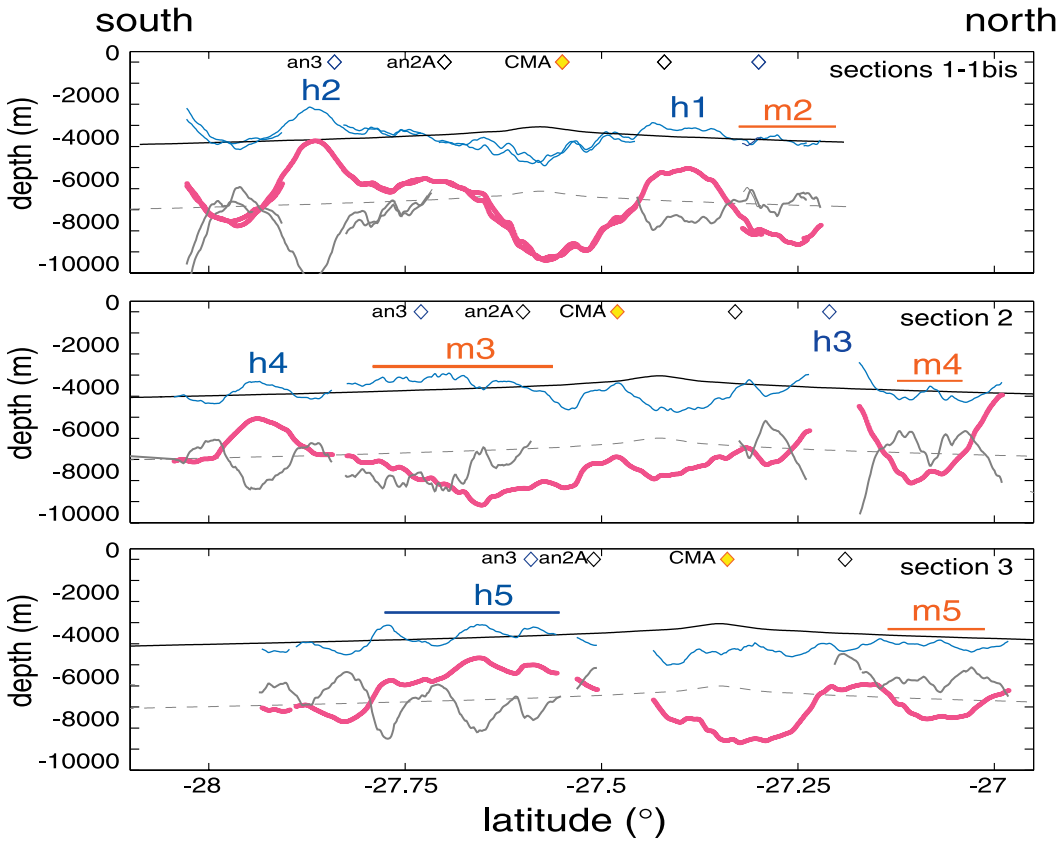

Figure 8. Across-axis sections 1-1bis, 2 and 3 in the 66°E area (see location on Figure 6). Sections 1 and 1b is Losanges show location of magnetic anomalies (CMA: central magnetic anomaly). Thin black line: topography predicted using *Parsons and Sclater* [1977] relationship (see caption for Figure 3). Blue line: actual seafloor topography. Pink line: Moho depth as predicted from gravity data. Thick gray line: Moho topography calculated for the case of perfect Airy compensation of seafloor topography (see Data Processing section). For this calculation, we considered only off-axis areas and made the hypothesis that topography predicted using the *Parsons and Sclater* [1977] relationship would be compensated by the reference 3000 m-thick crust used in our RMBA inversion. Thin dashed gray line: reference Moho depth (predicted using *Parsons and Sclater* [1977] topography + 3000 m). Red and blue letters refer to topographic and gravimetric features discussed in text and also shown in Figures 6 and 13.

gravity-derived crustal thicknesses up to ~7 km are found again some 40 km to the northeast of present-day segment #11, between magnetic anomalies 2A and 3A (topographic high noted as m8 in Figure 9d). Seafloor of similar age on the southern ridge flank, while even shallower (topographic high noted as h8 in Figure 9d), has a less negative RMBA signature (gravity-derived crustal thickness ~5 km). Topographic and crustal thickness variation patterns in the 64°E region are therefore similar to those observed in the 66°E region: short-scale crustal thickness variations, a common departure from isostatic compensation of seafloor topography, and a pronounced asymmetry of crustal thickness and seafloor relief between the two ridge flanks. Across-axis sections in Figure 11 illustrate the detail of these patterns.

[22] Section 1 crosses the axis ~12 km to the west of the center of segment #11 and cuts through the Fuji Dome, a dome-shaped domain that bears spreading parallel corrugations and is interpreted as the footwall of a fossil detachment fault [*Searle et al.*, 1999]. Topography over this dome is not compensated by thicker crust, nor are the topographic highs noted as h6 and h7 that occur in older seafloor further to the south (Figures 9 and 11). By contrast, two less pronounced topographic highs on the northern ridge flank, noted as m6 and m7, that formed at about the same age

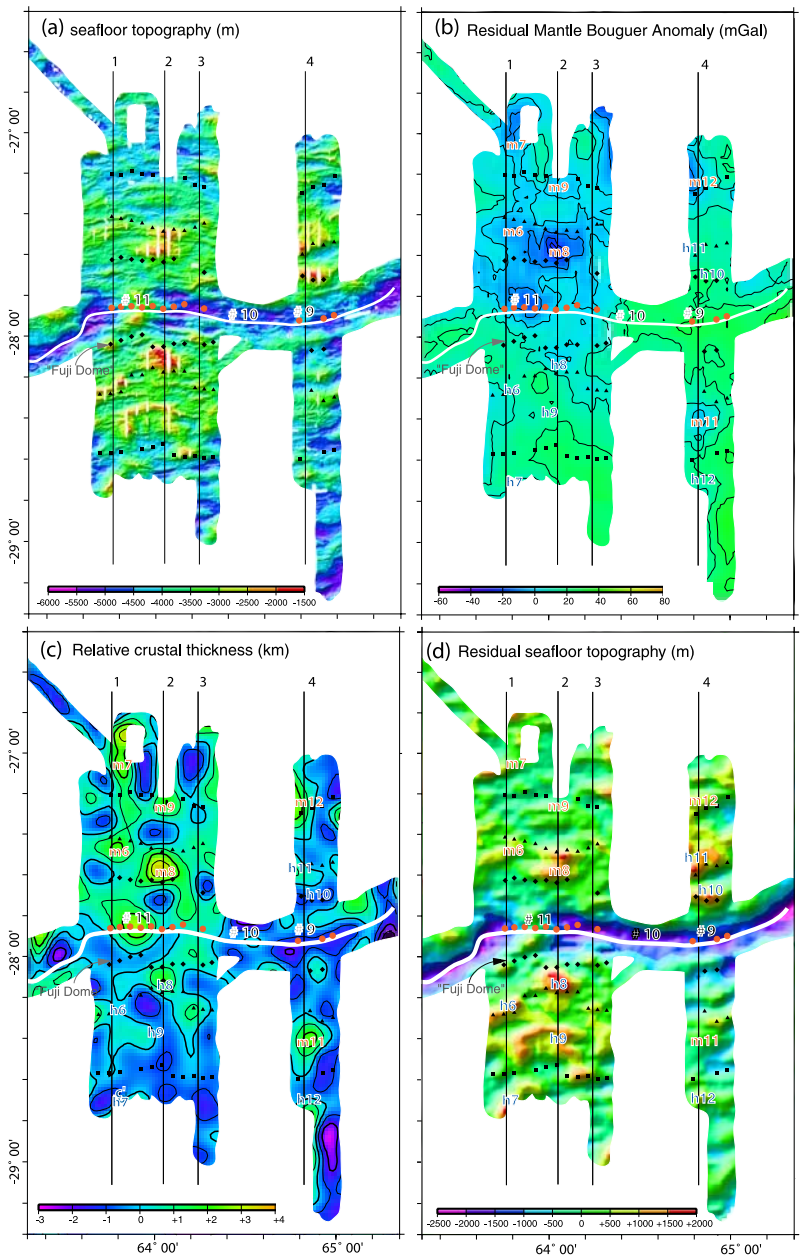

Figure 9. Maps of the 64°E area: (a) detail of Figure 1, showing only shipboard bathymetric data; (b) residual mantle Bouguer Anomaly obtained from shipboard FAA data (see section 2); (c) relative crustal thickness derived from RMBA map (see section 2); (d) detail of Figure 5, showing only residual topography from shipboard bathymetric data. White line: proposed location of present-day ridge axis [*Cannat et al.*, 1999]. Red dots: central magnetic anomaly; black losanges: magnetic anomaly 2A; black triangles: magnetic anomaly 3A; black squares: magnetic anomaly 5. Thin black lines noted as 1, 2, 3 and 4: location of sections shown in Figures 11 and 13. Letters in red and blue: topographic and gravimetric features discussed in text and also shown in Figures 11 and 13. Letters in red correspond to thicker crust domains; letters in blue correspond to topographic highs that are not associated with thicker than average crust (uncompensated highs).

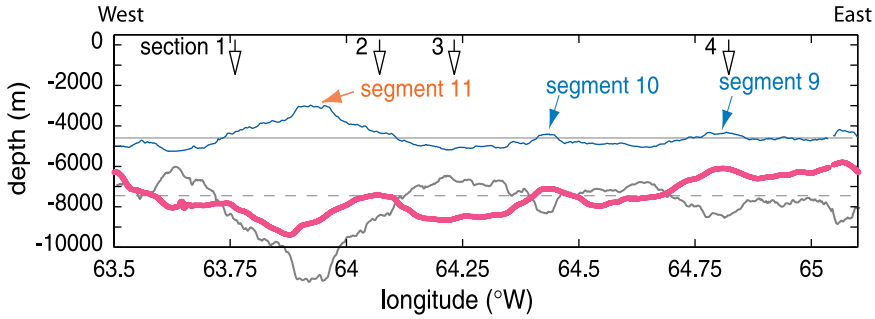

Figure 10. Section along central magnetic anomaly in the 64°E area (see Figure 9). Arrows show intersections with across-axis sections 1, 2, 3, and 4 (see Figure 11). Pink line: Moho depth as predicted from gravity data. Thick gray line: Moho topography calculated for the case of perfect Airy compensation of seafloor topography (see Data Processing section). For this calculation, we made the hypothesis that seafloor lying at the mean axial depth in the 64°E area (thin gray line: 4720 m; calculated for axis as defined in Figure 9) would be compensated by the mean gravity-derived axial crustal thickness in the 64°E area (2900 m; also calculated for axis as defined in Figure 9). Thin dashed gray line: reference Moho depth (4720 + 2900 m).

as topographic highs h6 (around the time of magnetic anomaly 2A) and h7 (before the time of anomaly 5), respectively, correspond to somewhat thickened crust (gravity-derived crustal thickness 5.4 km and 4.7 km, respectively).

[23] Section 2 in Figure 11 crosses the axis ~20 km to the east of the center of segment #11 and shows the contrast in gravity-derived crustal thickness between topographic highs m8 and h8 (~7 km and ~5 km, respectively), formed between magnetic anomalies 2A and 3A, and between topographic high h9 and the low-relief feature noted as m9, formed between magnetic anomalies 3A and 5. In both cases, the thicker crust is found on the northern ridge flank, and topographic highs on the southern ridge flank are uncompensated features.

[24] Section 3 in Figure 11 crosses the axis at the eastern end of segment #11. It stands out in that it shows little across-axis variations of seafloor topography and gravity-derived crustal thickness, at least for crust younger than magnetic anomaly 5. Seafloor topography fits the calculated subsidence curve well, while gravity-derived crustal thickness is close to the reference 3 km value used in our inversion of RMBA data.

[25] Section 4 in Figure 11 crosses the axis near the center of segment #9. It shows large across-axis variation of seafloor topography and gravity-derived crustal thickness, and a pronounced asymmetry between the two ridge flanks. Topographic highs are found on the northern ridge flank, and the highest ones (h10 and h11) are underlain by thinner than average crust and are therefore uncompensated. Topographic high h10 on the northern ridge flank is similar to topographic high h1 in the 66°E area (Figure 8) in that crust of equivalent age on the southern ridge flank is also thin (Figure 11). Topographic high m12, formed around the time of magnetic anomaly 5, is less prominent than topographic highs h10 and h11 and underlain by thicker than average crust (gravity-derived crustal thickness ~5 km). Crust of similar age on the southern ridge flank is thin and corresponds to relief h12. Topographic high h11 is located near our pickings for magnetic anomaly 3A. Crust of similar age on the southern ridge flank is thicker than average (seafloor domain noted as m11; gravity-derived crustal thickness ~5 km).

6. Discussion

6.1. Focused Melt Supply to the Easternmost SWIR

[26] Crustal thickness, as derived from seismic data in the 66°E SWIR region, varies between ~2.5 km, and more than 6 km [*Muller et al.*, 1999] (Figure 4). Our gravity-derived crustal thickness estimates for the 66°E and 64°E regions range from values <2 km, which we view as underestimates of true crustal thickness based on comparison with seismic results (Figure 4), and ~7 km. This range of

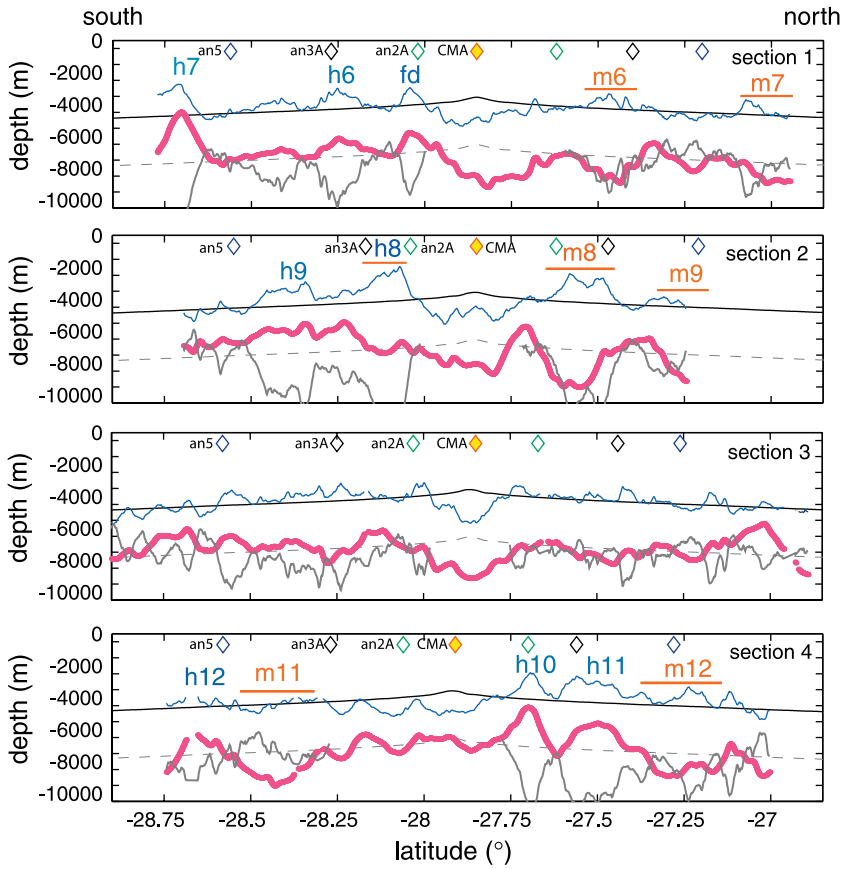

Figure 11. Across-axis sections 1, 2, 3, and 4 in the 64°E area (see location on Figure 9). Losanges show location of magnetic anomalies (CMA: central magnetic anomaly). Thin black line: topography predicted using the *Parsons and Sclater* [1977] relationship (see caption for Figure 3). Blue line: actual seafloor topography. Pink line: Moho depth as predicted from gravity data. Thick gray line: Moho topography calculated for the case of perfect Airy compensation of seafloor topography (see section 2). For this calculation, we considered only off-axis areas and made the hypothesis that topography predicted using the *Parsons and Sclater* [1977] relationship would be compensated by the reference 3000 m-thick crust used in our RMBA inversion. Thin dashed gray line: reference Moho depth (predicted using *Parsons and Sclater* [1977] topography + 3000 m). fd: Fuji Dome. Red and blue letters refer to topographic and gravimetric features discussed in text and also shown in Figures 9 and 13.

variation is comparable to that observed at the MAR [*Hooft et al.*, 2000; *Tolstoy et al.*, 1993; *Wolfe et al.*, 1995], but the average seismic crustal thickness in the 66°E SWIR region, based on the CAM116 seismic profile, is smaller than at the MAR (~3.7 km versus ~6 km). The average seismic crustal thickness along the CAM116 profile is also smaller than the average seismic crustal thickness for segment 8 (4.7 km; Table 1). Similarly, the mean gravity-derived axial crustal thickness for segment 11 (3.9 km) is larger than the mean gravity-derived axial crustal thickness in the 64°E area (2.9 km). As stressed in the introduction of this paper, this suggests that while each MAR segment is supplied with close to the regional average amount of melt, thick crust segments of our SWIR study area receive more melt than the regional average.

[27] Large crustal thickness variations, as deduced from gravity data, also occur faster in our SWIR study area than at the MAR, and ridge segmentation patterns are more unstable. Melt distribution in our SWIR study area is therefore both more irregular in space, and more variable in time, than at the MAR. This first part of the discussion summarizes the characteristics of melt focusing in our SWIR study area, then addresses the mecha-

nisms that could govern such focused and transient melt supply.

6.1.1. Characteristics of Melt Distribution at the Easternmost SWIR

[28] The two studied SWIR regions (Figures 6 and 9) are contiguous and total ~350 km in ridge length. In these two regions, there are only two present-day segments (#8 in the 66°E region and #11 in the 64°E region) with maximum gravity-derived crustal thicknesses >5.5 km. Two present-day segments (#6 and #7 in the 66°E region) have maximum gravity-derived crustal thicknesses between 4 and 5.5 km, while the other two identified present-day segments (#9 and #10 in the 64°E region) have gravity-derived crustal thicknesses less than the reference 3 km used in the gravity model.

[29] The off-axis coverage of our study area is not complete, but existing off-axis data suggest that past and present-day crustal thickness variation patterns are consistent. There are only two off-axis domains (noted as m3 in Figure 6 and m8 in Figure 9), with gravity-derived crustal thickness >5.5 km, and eight off-axis domains (noted as m2 and m4 in Figure 6 and m6, m7, h8, m9, m11, and m12 in Figure 9), with gravity-derived crustal thicknesses between 4 and 5.5 km. These domains extend 20 to 40 km in the along-axis and across-axis directions (Figures 6 and 9). They represent ~10% of the area mapped in the 66°E region, and ~14% of the area mapped in the 64°E region. If thick crust was emplaced strictly on axis, and given that the thicker crust domains do not appear to have formed repeatedly at the same locations along the axis, this would suggest that, at any point along the ridge, melt supply to the crust has been significantly enhanced ~10–15% of the time, over the past 10 myr.

[30] On axis domains with thick crust, such as segments #8 and 11, look like large volcanoes that fill the axial valley [*Cannat et al.*, 1999]. Formation of such edifices may have involved outpouring of lavas over previously accreted lithosphere. Thick crust domains may therefore have formed faster than suggested by their along flow line dimensions (20 to 40 km, corresponding to ~1.3 to 2.7 myr assuming a spreading rate of 15 mm/yr). The relative duration of enhanced melt supply episodes in our study area could then be less than ~10 to 15% of the time.

[31] The estimated volume of excess crust emplaced at the center of present-day segment #11 (Figures 9 and 10), relative to the reference crustal thickness value of 3 km used in our gravity model, is ~600 km^3 (volume measured within the +1 km contour in the gravity-derived relative crustal thickness map of Figure 9c). The estimated excess crustal volume of nearby off-axis thick crust domain m8 (Figures 9 and 11) is similar, but total excess crust emplaced at the axis when this domain was formed (between magnetic anomalies 2A and 3A; Figure 9) was of the order of ~850 km^3 (excess crust in domain m8 + excess crust in domain h8). It seems safe to assume that the excess crustal material in thick crust domains formed from excess basaltic melts, but two questions remain open: (1) how fast were these excess melts emplaced, and (2) how much melt-derived material, relative to serpentinized mantle-derived material, is there in the crust of our study area? These two questions condition the quantitative evaluation of along-axis melt focusing in the easternmost SWIR.

[32] As discussed earlier, it is possible that thick crust domains formed faster than suggested by their along flow line dimensions. The extent of melt focusing during the formation of thick crust domains may thus be greater than suggested by the mere comparison of the excess crustal volume in thick crust domains (~600 km^3) with the volume (~2900 km^3) of a 3 km-thick crustal block with similar along-axis (30 km), and across-axis (30 km, equivalent to ~2 myr of spreading) extension. For example, if the ~600 km^3 excess melt were emplaced over 0.5 myr only, the volume of crust accreted in a 30 km-long and 3 km-thick crustal block during the same period would be ~700 km^3. In addition, it is possible that thin crust domains of the SWIR comprise a significant proportion of variably serpentinized mantle-derived peridotites [*Fujimoto et al.*, 1999; *Mével et al.*, 1997]. Thick crust segments of the eastern SWIR may therefore receive more than twice the amount

of melt that is delivered to thin crust areas during the same period.

6.1.2. Possible Melt-Focusing Mechanisms

[33] Four mechanisms have been described to explain melt focusing along mid-ocean ridges: (1) melting of hotter or enriched mantle [*Bonatti*, 1990; *Klein and Langmuir*, 1987]; (2) diapiric instabilities in the subaxial mantle [*Lin et al.*, 1990; *Sparks et al.*, 1993]; (3) instabilities in melt delivery due to melt extraction mechanisms in the melting region [*Scott and Stevenson*, 1986]; and (4) along-axis migration of melt at the base of the lithosphere [*Magde and Sparks*, 1997].

[34] Mechanisms 1 and 2 should induce specific chemical signatures in the basalts from thicker crust segments [*Langmuir et al.*, 1992]. There is no evidence for this in the basalts collected in our study area [*Humler et al.*, 1998; *Meyzen et al.*, 2003]. The sampling interval, however, is relatively large (~20 to 30 km except for the center of segment #11) so that we do not at this stage rule out mantle heterogeneity, or mantle diapirs, as causes of enhanced melt supply events in our study area. Given the small along-axis extension (~30 km), and short duration (<3 myr) of these enhanced melt supply events, enriched or hotter mantle domains would, however, have to be small (a few tens of km at most in the along-axis and vertical dimensions). Given the expected efficiency of heat transfer in the convecting mantle, this appears to rule out the hotter mantle interpretation. Mantle diapirs would also have to be small in diameter, short-lived, and randomly distributed along-axis.

[35] Instabilities in melt delivery to the ridge axis (mechanism 3) have been modeled in the form of solitary waves of high porosity, with a high melt content, also called "magmons" [*Rabinowicz et al.*, 2001; *Scott and Stevenson*, 1986], that could grow and rise due to porous flow of melt and compaction of the mantle matrix in the melting region. Mechanism 4 is a variation on a model proposed by [*Sparks and Parmentier*, 1991], that explained across-axis focusing of melt toward mid-ocean ridges by gravity-driven melt migration in a porous boundary layer at the base of the cooling lithosphere (just below the melt's liquidus). [*Magde and Sparks*, 1997] proposed that melt could also flow along-axis toward the center of MAR segments, following the sloping base of the axial lithosphere from segment ends (thick lithosphere), to segment center (thinner lithosphere). Melt focusing along the SWIR to the east of the Melville FZ could be due to a similar mechanism, but two important differences would have to be accounted for: segments of the MAR commonly persist for 10 to 20 myr [*Gente et al.*, 1995; *Rommevaux et al.*, 1994; *Tucholke et al.*, 1997], while most segments of the easternmost SWIR do not persist for more than 2 to 3 myr. Also, as mentioned previously, because thicker crust segments of the SWIR receive more melt than the regional average, along-axis melt migration would have to occur over a ridge length greater than the length of these segments, and/or over periods longer than the time required to form the thicker crust segments.

[36] On the basis of along-axis bathymetric and gravimetric data, *Cannat et al.* [1999] proposed that thicker crust segments of the SWIR could result from a combination of melt migration near the base of the lithosphere and rapid melt extraction through dikes rooted in melt-rich regions. Our off-axis observations allow us to refine this hypothesis, as sketched in Figure 12. In this cartoon, topography of the base of the axial lithosphere (required to trigger along-axis melt migration) is initiated by a localized increase in melt supply (caused by a short-lived diapiric instability in the mantle, an isolated "magmon," or by melting of a small domain of enriched mantle). Most melts that reach the base of the lithosphere are likely to have been extracted from the mantle at some depth within the melting region, and should therefore be warmer than the surrounding mantle. The base of the lithosphere should therefore be thermally eroded wherever most melts have gathered. These melts may also experience limited crystallization, and release latent heat. An alternative way of creating a topography along the base of the lithosphere, proposed by *Magde and Sparks* [1997] for the MAR case, is that cooling of the lithosphere is enhanced near ridge offsets (more pervasive

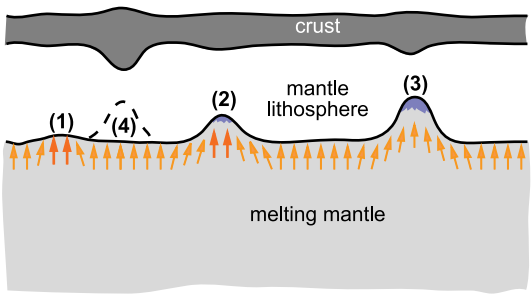

Figure 12. Cartoon showing proposed four stages in the growth of thicker crust domains at the axis of the SWIR to the east of the Melville FZ. Along-axis section (not to scale) through the crust (dark gray), the thick mantle lithosphere (white), and the melting upper mantle (pale gray). Yellow and red arrows figure the flux of melt at the top of the melting region. Red arrows indicate enhanced melt supply from the mantle. At stage (1), enhanced melt supply initiates local thermal thinning of the base of the axial lithosphere, creating a topography that allows melt migration from neighboring regions. At stages (2) and (3), thermal thinning and melt migration are enhanced. A melt-rich region (in blue) develops and increased magmatism thickens the crust. Enhanced melt supply from the mantle may or may not persist during stages (2) and (3). At stage (4), the melt-rich region has been tapped by dikes feeding volcanism in the crust, the axial lithosphere has returned to its original thickness and along-axis melt migration has consequently ceased. See text for further discussion.

faulting plus cooling edge effect of offset [*Fox and Gallo*, 1984]). This explanation does not, however, fit our SWIR study area, because axial valley walls there are very continuous, with few detectable offsets [*Mendel et al.*, 1997] (Figures 6a and 9a).

[37] Once topography is created at the base of the lithosphere, melts should migrate along this sloping horizon [*Sparks and Parmentier*, 1991], and gather beneath what then becomes the center of a thick crust ridge segment (Figure 12, Stages 2 and 3). This setup could in principle be self maintained, melt migration toward the segment center providing the heat required to keep the lithosphere thin at this location. Thicker crust segments of our SWIR study area, however, are short-lived and there must therefore be a mechanism by which the lithosphere at segment center rapidly cools back to its original thickness (Stage 4; Figure 12). We propose that rapid melt extraction by dikes rooting in the melt-rich region [*Sleep*, 1988], followed by the disruption of the volcanic edifices by faults that reach deep into the axial lithosphere and channel hydrothermal fluids, may be the cause of such rapid cooling.

[38] This model fits the observations presented in this paper and has the asset of making use of a likely characteristic of ultra-slow spreading: the presence of a thick axial lithospheric lid. It is compatible with the existence of small scale heterogeneities, both compositional [*Seyler et al.*, 2003] and dynamic, in the mantle of this ultra-slow ridge. This model needs, however, to be tested in quantitative models (Can melts effectively thin a thick axial lithosphere at sufficient rates? Can melts pool beneath this lithospheric lid at segment centers and be rapidly extracted to build the large volcanoes observed at the seafloor? Can rapid melt extraction and faulting cause the axial lithosphere to thicken at a sufficient rate?) and to be evaluated using new seismic, geological, and basalt chemistry data.

6.2. Tectonically Maintained Topography and the Modes of Crustal Accretion Outside Periods of Higher Than Average Melt Supply

[39] Along-axis seafloor topography at the MAR appears nearly compensated by coincident variations in crustal thickness [*Escartin and Lin*, 1998; *Lin et al.*, 1990; *Neumann and Forsyth*, 1993]. This is not the case in our SWIR study area. Furthermore, off-axis seafloor topography and gravity-derived Moho topography in our SWIR study area are more commonly correlated than anti-correlated: many topographic highs are underlain by thin crust, and thick crust areas commonly correspond with deep seafloor. This indicates that, for the most part, seafloor topography in our SWIR study area is tectonically maintained. The following discussion concerns the origin of this topography, and addresses the modes of crustal accretion that prevail in this easternmost region of the SWIR, whenever the melt supply to the axis is average to lower than average.

[40] Figure 13a shows two reconstructions of earlier across-axis configurations, for section 2 of Figure 8. Just after the time of anomaly 3, thicker crust domains m3 and m4 are juxtaposed, forming

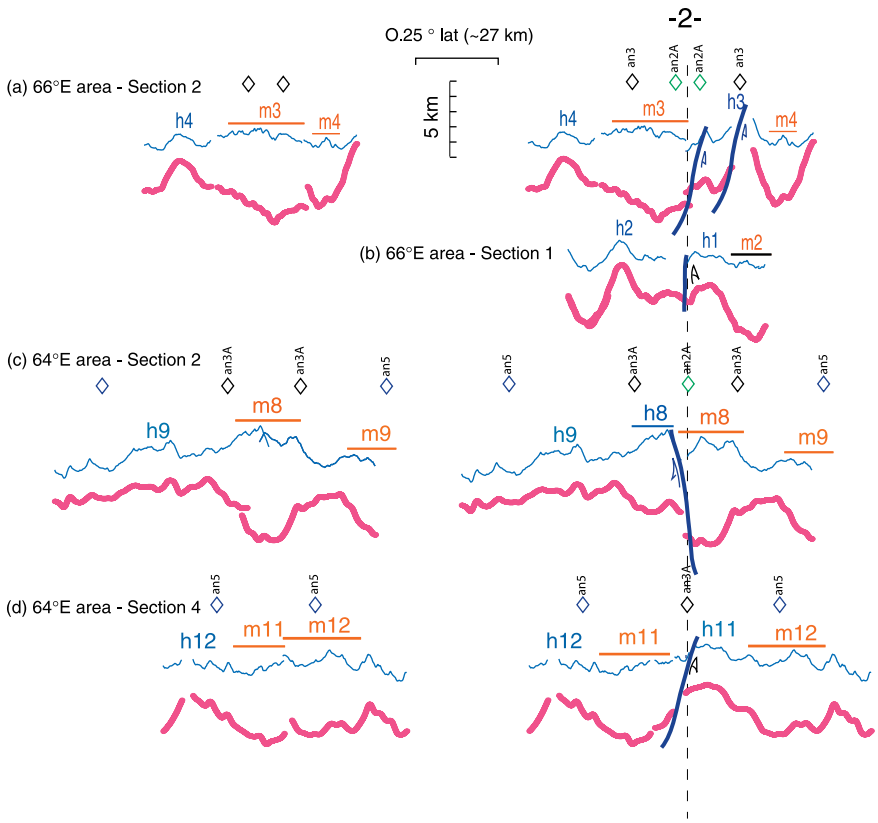

Figure 13. Reconstructions of earlier across-axis configurations (dashed vertical line: axis location). (a) and (b) for sections 2 and 1 in the 66°E area (see location in Figure 6 and present-day configuration in Figure 8). (c) and (d) for sections 2 and 4 in the 64°E area (see location in Figure 9 and present-day configuration in Figure 11). Losanges show location of magnetic anomalies. Blue line: present-day seafloor topography. Pink line: Moho depth as predicted from gravity data. Red and blue letters refer to topographic and gravimetric features discussed in text and also shown in Figures 6, 8, 9, and 11. Letters in red correspond to thicker crust domains; letters in blue correspond to topographic highs that are not associated with thicker than average crust (uncompensated highs). Left-hand panel corresponds to times of enhanced melt supply and emplacement of thicker crust domains. Right-hand panel corresponds to times of low melt supply and faulting of formerly emplaced thicker crust domains. See text for details.

a single, 36 km-wide thicker crust domain (Figure 13a, left-hand panel). Spreading then jumps to the northern side of this wide thicker crust domain, creating thinner crust with seafloor parallel gravity-derived Moho topography (Figure 13a, right-hand panel). This pattern, with highest reliefs corresponding with upward warping of the Moho, is characteristic of fault blocks. The Fuji Dome, that bears spreading parallel corrugations and is interpreted as the flexured footwall of a fossil detachment fault surface [*Searle et al.*, 1999], shows this same upward warping pattern in section 1 of Figure 11.

[41] Figure 13b shows a reconstruction for Section 1 of Figure 8, at the same time as the reconstruction shown in the right-hand panel of Figure 13a. The uncompensated relief h1 in the northern ridge flank is juxtaposed with deeper, similarly thin crusted seafloor in the southern ridge flank. A similar configuration is found in Section 4 of Figure 11 between the uncompensated relief h11 to the north, and deeper and thin crusted seafloor to the south. We interpret this configuration as due to footwall uplift associated to asymmetric normal faulting of a thin crust domain.

[42] Figure 13c shows reconstructed across-axis configurations for Section 2 of Figure 11: thicker crust domains m8 and h8 are juxtaposed just before the time of anomaly 2A, forming a single thicker crust domain (Figure 13c, left-hand panel); at the

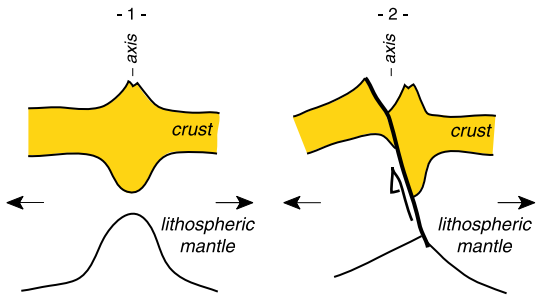

Figure 14. SWIR to the east of the Melville FZ. Cartoon showing across-axis sections (not to scale) sketched after the reconstructed across-axis configurations of Figure 13. Left-hand panel (1) corresponds to a time of enhanced melt supply and emplacement of thicker crust domains (stage 3 in Figure 12). Right-hand panel (2) corresponds to a time of low melt supply and asymmetric faulting of the formerly emplaced thicker crust domain (stage 4 in Figure 12).

time of anomaly 2A (Figure 13c, right-hand panel), the reconstructed profile is consistent with the existence of a north dipping normal fault, which could have accommodated most of the noncompensated topography of thicker crust domain h8 (see section 2 in Figure 11).

[43] Figure 13d shows the evolution of Section 4 of Figure 11: a little after the time of anomaly 5, thicker crust domain m11 is on axis (Figure 13d, left-hand panel); at the time of anomaly 3A, spreading has jumped to the north side of this thicker crust domain, forming the uncompensated relief h11, which we interpret as the flexured footwall of a large south dipping normal fault (Figure 13d, right-hand panel). A reconstruction made for this same section at the time of anomaly 5 would have shown a similar pattern, but with a large north dipping normal fault separating thicker crust domain m12, from uncompensated relief h12 (see Figure 11). Similarly, at the time of anomaly 3, section 1 of Figure 8 juxtaposes thicker crust domain m2, and the prominent uncompensated relief h2, possibly along a large north dipping normal fault.

[44] The pattern that emerges from the reconstructions shown in Figure 13, and from the sections shown in Figures 8 and 11, is therefore one in which spreading with average, to lower than average, melt supply is dominated by normal faulting, producing prominent uncompensated reliefs, seafloor-parallel Moho topography, and a pronounced asymmetry in topography and crustal thickness between the two ridge flanks. Reconstructed across-axis sections (Figure 13) suggest that this asymmetry arises both because faults tend to initiate on the sides and not in the center of thicker crust domains (Figure 14), and because large offset faulting produces significant flexural uplift in the footwalls. Producing large faults and maintaining high uncompensated reliefs requires the axial lithosphere to be thick. A thick lithosphere is a predictable characteristic for this ultra-slow ridge, that has an anomalously low regionally averaged melt supply. This is consistent with hypocenters depths up to 12 km that have been recorded during a 45 days passive OBS experiment at segment #11 [*Yamada et al.*, 2002].

7. Conclusions

[45] The SWIR in our study area (63°E to 67°E) is characterized by large crustal thickness variations over distances of a few tens of km both along and across-axis. Melt supply to the ridge appears more focused than at the faster spreading MAR, thicker crust segments receiving more melt than the regional average. Thicker crust segments of the SWIR are also substantially shorter lived than segments of the MAR. Recent data show that the ultra-slow Gakkel ridge in the Arctic could share these characteristics [*Cochran et al.*, 2003; *Dick et al.*, 2001; *Kurras et al.*, 2001]. In our discussion, we propose a model for such strong and transient melt focusing that involves localized and transient increases in the volume of melt that is supplied to the base of the axial lithosphere, melt migration along the base of this lithosphere to the center of thicker crust segments, and rapid extraction of these melts by dikes that feed large volcanic constructions on the seafloor. We view this model as a preliminary attempt at understanding the peculiar characteristics of the SWIR in its easternmost portion, that will have to be tested using modeling and the acquisition of more data.

[46] The SWIR in our study area is also characterized by a general departure from isostatic compen-

sation of seafloor topography, and by a pronounced asymmetry of crustal thickness and seafloor relief between the two ridge flanks. At the faster spreading MAR, these characteristics are found near transform or nontransform discontinuities. Comparing seafloor topography and gravity-derived Moho topography in across-axis sections leads us to propose that spreading during periods when the ridge does not receive a high melt supply is dominated by asymmetric normal faulting, with significant flexural uplift of the footwalls. These periods of low melt supply represent most of the time in our easternmost SWIR study area: ~85% of the seafloor in the 66°E and 64°E areas (Figures 6c and 9c) corresponds with gravity-derived relative crustal thicknesses <4 km.

[47] Faults dip either to the north or to the south, and changes in fault polarity appear frequent, both along axis, and across-axis (i.e., with time) along a given flow line. We are confident that our interpretation in terms of large offset normal faulting is robust because it fits the data presented here and the predictable existence of a very thick lithosphere at this ultra-slow and magma-starved ridge. This interpretation is also consistent with the widespread emplacement of variably serpentinized peridotites at the seafloor, as observed in dredging and submersible data [*Fujimoto et al.*, 1999; *Mével et al.*, 1997]. Further work, including modeling and the acquisition of additional data, is required, however, to understand the dynamics of these faults, how deep they reach, and what causes them to switch polarity.

Acknowledgments

[48] We gratefully acknowledge the work of the RV Yokosuka crew and of the scientific party during the Mode'98 Leg 3 INDOYO cruise. This work also benefited from discussions with many colleagues involved in previous cruises to the SWIR. We particularly thank Daniel Sauter and Catherine Mével for their work as guest editors, Roger Buck and an anonymous referee for their helpful reviews, and Javier Escartin for his comments on an early draft of the paper. This is IPGP contribution 1897.

References

Bonatti, E., Not so hot "hot spots" in the oceanic mantle, *Science*, *250*(4977), 107–111, 1990.

Canales, J. P., R. S. Detrick, J. Lin, J. A. Collins, and D. R. Toomey, Crustal and upper mantle seismic structure beneath the rift mountains and across a non-transform offset at the Mid-Atlantic Ridge (35°N), *J. Geophys. Res.*, *105*(B2), 2699–2719, 2000.

Cande, S. C., and D. V. Kent, Revised calibration of the geomagnetic polarity timescale for the Late Cretaceous and the Cenozoic, *J. Geophys. Res.*, *100*, 6093–6095, 1995.

Cannat, M., C. Rommevaux-Jestin, D. Sauter, C. Deplus, and V. Mendel, Formation of the axial relief at the very slow spreading Southwest Indian Ridge (49°–69°E), *J. Geophys. Res.*, *104*(B10), 22,825–22,843, 1999.

Cochran, J. R., G. J. Kurras, M. H. Edwards, and B. J. Coakley, The Gakkel Ridge: Bathymetry, gravity anomalies, and crustal accretion at extremely slow spreading rates, *J. Geophys. Res.*, *108*(B2), 2116, doi:10.1029/2002JB001830, 2003.

Detrick, R. S., R. S. White, and G. M. Purdy, Crustal structure of North Atlantic fracture zones, *Rev. Geophys.*, *31*(4), 439–459, 1993.

Dick, H. J. B., G. J. Kurras, J. E. Snow, W. Jokat, P. J. Michael, and C. H. Langmuir, Volcanic and tectonic processes along the Gakkel Ridge: Morphologic interpretation of axial valley features and samples from the Arctic Mid-Ocean Ridge Expedition (AMORE 2001), *Eos Trans. AGU*, *82*(47), Fall Meet. Suppl., abstract T11B-0856, 2001.

Escartin, J., and J. Lin, Tectonic modification of axial crustal structure: Evidence from spectral analyses of residual gravity and bathymetry of the Mid-Atlantic Ridge flanks, *Earth Planet. Sci. Lett.*, *154*(1–4), 279–293, 1998.

Fox, P. J., and D. G. Gallo, A tectonic model for Ridge-transform-Ridge plate boundaries: Implications for the structure of oceanic lithosphere, *Tectonophysics*, *104*, 205–242, 1984.

Fujimoto, H., et al., First submersible investigations of mid-ocean ridges in the Indian Ocean, *InterRidge News*, *8*(1), 22–24, 1999.

Gente, P., R. A. Pockalny, C. Durand, C. Deplus, M. Maia, G. Ceuleneer, C. Mevel, M. Cannat, and C. Laverne, Characteristics and evolution of the segmentation of the Mid-Atlantic Ridge between 20°N and 24°N during the last 10 million years, *Earth Planet. Sci. Lett.*, *129*, 55–71, 1995.

Hooft, E. E. E., R. S. Detrick, D. R. Toomey, J. A. Collins, and J. Lin, Crustal thickness and structure along three contrasting segments of the Mid-Atlantic Ridge, 33.5°–35°N, *J. Geophys. Res.*, *105*, 8205–8226, 2000.

Humler, E., C. M. Meyzen, J. N. Ludden, and C. Mével, Geochemical variations in basaltic glasses from the Southwest Indian Ridge (49 to 70°E), *Eos Trans. AGU*, *79*(45), Fall Meet., Suppl., F878, 1998.

International Association of Geomagnetism and Aeronomy, Division V, Working Group 8, M. Mandea, S. Macmillan, T. Bondar, V. Golovkov, B. Langlais, F. Lowes, N. Olsen, J. Quinn, and T. Sabaka, International geomagnetic reference field—2000, *Phys. Earth Planet. Inter.*, *120*, 39–42, 2000.

Klein, E. M., and C. H. Langmuir, Global correlations of ocean ridge basalt chemistry with axial depth and crustal chemistry, *J. Geophys. Res.*, *92*, 8089–8115, 1987.

Kuo, B. Y., and D. W. Forsyth, Gravity anomalies of the ridge-transform system in the South Atlantic between 31° and 34.5°S: Upwelling centers and variation in crustal thickness, *Mar. Geophys. Res.*, *10*, 205–232, 1988.

Kurras, G. J., S. Gauger, P. J. Michael, J. Thiede, H. J. B. Dick, T. Hartmann, J. Hatzky, W. Jokat, and C. H. Langmuir, Axial valley morphology of the Gakkel ridge [8°W–88°E]: Seabeam and hydrosweep bathymetry from the Arctic Mid-Ocean Ridge Expedition (AMORE 2001), *Eos Trans. AGU*, *82*(47), Fall Meet. Suppl., abstract T11B-0855, 2001.

Langmuir, C. H., E. M. Klein, and T. Plank, Petrological systematics of mid-ocean ridge basalts: Constraints on melt generation beneath ocean ridges, in *Mantle Flow and Melt Generation at Mid-Ocean Ridges*, *Geophys. Monogr. Ser.*, vol. 71, edited by J. Phipps Morgan, D. K. Blackman, and J. M. Sinton, pp. 183–280, AGU, Washington, D. C., 1992.

Lin, J., G. M. Purdy, H. Schouten, J.-C. Sempéré, and C. Zervas, Evidence for focused magmatic accretion along the Mid-Atlantic Ridge, *Nature*, *344*, 627–632, 1990.

Magde, L. S., and D. W. Sparks, Three-dimensional mantle upwelling, melt generation, and melt migration beneath segments of slow spreading ridges, *J. Geophys. Res.*, *102*(B9), 20,571–20,583, 1997.

Mendel, V., D. Sauter, L. Parson, and J.-R. Vanney, Segmentation and morphotectonic variations along a super-slow spreading center: The Southwest Indian Ridge (57°E–70°E), *Mar. Geophys. Res.*, *19*, 505–533, 1997.

Mével, C., et al., Sampling the Southwest Indian Ridge: First results of the EDUL cruise (R/V Marion Dufresne II, August 1997), *InterRidge News*, *6*(2), 25–26, 1997.

Meyzen, C. M., M. J. Toplis, E. Humler, J. N. Ludden, and C. Mével, A discontinuity in mantle composition beneath the Southwest Indian Ridge, *Nature*, *421*(6924), 731–733, 2003.

Muller, M. R., T. A. Minshull, and R. S. White, Segmentation and melt supply at the Southwest Indian Ridge, *Geology*, *27*(10), 867–870, 1999.

Munschy, M., Etude géophysique détaillée du point triple de Rodriguez et de la zone axiale des trois dorsales associées, doctorate thesis, Univ. Louis Pasteur, Strasbourg, France, 1987.

Munschy, M., and R. Schlich, The Rodriguez Triple Junction (Indian ocean): Structure and evolution for the past one million years, *Mar. Geophys. Res.*, *11*, 1–14, 1989.

Neumann, G. A., and D. W. Forsyth, The paradox of the axial profile: Isostatic compensation along the axis of the Mid-Atlantic Ridge?, *J. Geophys. Res.*, *98*(B10), 17,891–17,910, 1993.

Okino, K., D. Curwitz, M. Asada, K. Tamaki, P. Vogt, and K. Crane, Preliminary analysis of the Knipovich Ridge segmentation: Influence of focused magmatism and ridge obliquity on an ultraslow spreading system, *Earth Planet. Sci. Lett.*, *202*, 275–288, 2002.

Parson, L. M., D. Sauter, V. Mendel, P. Patriat, and R. C. Searle, Evolution of the axial geometry of the southwest Indian Ocean ridge between the Melville Fracture Zone and the Indian Ocean Triple Junction—Implications for segmentation on very slow-spreading ridges, *Mar. Geophys. Res.*, *19*, 535–552, 1997.

Parsons, B., and J. G. Sclater, An analysis of the variation of ocean floor bathymetry and heat flow with age, *J. Geophys. Res.*, *82*, 803–827, 1977.

Patriat, P., and J. Segoufin, Reconstruction of the Central Indian Ocean, *Tectonophysics*, *155*, 211–234, 1988.

Rabinowicz, M., P. Genthon, G. Ceuleneer, and M. Hillairet, Compaction in a mantle mush with high melt concentrations and the generation of magma chambers, *Earth Planet. Sci. Lett.*, *188*, 313–328, 2001.

Rommevaux, C., C. Deplus, P. Patriat, and J.-C. Sempéré, Three-dimensional gravity study of the Mid-Atlantic Ridge: Evolution of the segmentation between 28° and 29°N during the last 10 m.y., *J. Geophys. Res.*, *99*(B2), 3015–3029, 1994.

Rommevaux-Jestin, C., C. Deplus, and P. Patriat, Mantle Bouguer anomaly along an ultra-slow spreading ridge: Implications for accretionary processes and comparison with results from Central Mid-Atlantic Ridge, *Mar. Geophys. Res.*, *19*, 481–503, 1997.

Schlich, R., M. Munschy, J.-M. Marthelot, J.-Y. Royer, and M. Schaming, Les campagnes du N. O. Jean Charcot sur le point triple de Rodriguez (océan Indien): Premiers résultats, *Bull. Soc. Geol. France*, *8*, 693–697, 1987.

Scott, D., and D. Stevenson, Magma ascent by porous flow., *J. Geophys. Res.*, *91*, 9283–9296, 1986.

Searle, R. C., K. Fujioka, M. Cannat, C. Mével, H. Fujimoto, and L. M. Parson, FUJI Dome: A large detachment fault near 64 degrees E on the very slow spreading South West Indian Ridge, *Eos Trans. AGU*, *80*(46), Fall Meet. Suppl., F956, 1999.

Seyler, M., M. Cannat, and C. Mével, Evidence for major-element heterogeneity in the mantle source of abyssal peridotites from the Southwest Indian Ridge (52° to 68°E), *Geochem. Geophys. Geosyst.*, *4*(2), 9101, doi:10.1029/2002GC000305, 2003.

Sleep, N. H., Tapping of melt by veins and dikes, *J. Geophys. Res.*, *93*, 10,255–10,272, 1988.

Smith, D. K., and J. R. Cann, Constructing the upper crust of the Mid-Atlantic Ridge: A reinterpretation based on the Puna Ridge, Kilauea volcano, *J. Geophys. Res.*, *104*(B11), 25,379–25,399, 1999.

Smith, W. H., and D. T. Sandwell, Global seafloor topography from satellite altimetry and ship depth soundings, *Science*, *227*, 1956–1962, 1997.

Sparks, D. W., and E. M. Parmentier, Melt extraction from the mantle beneath spreading centers, *Earth Planet. Sci. Lett.*, *105*, 368–377, 1991.

Sparks, D. W., E. M. Parmentier, and J. Phipps Morgan, Three-dimensional mantle convection beneath a segmented spreading center: Implications for along axis variations in crustal thickness and gravity, *J. Geophys. Res.*, *98*, 21,977–21,995, 1993.

Tolstoy, M., A. J. Harding, and J. A. Orcutt, Crustal thickness on the Mid-Atlantic Ridge: Bull's eye gravity anomalies and focused accretion, *Science*, *262*, 726–729, 1993.

Tucholke, B. E., J. Lin, M. C. Kleinrock, M. Tivey, T. B. Reed, J. Goff, and G. E. Jaroslow, Segmentation and crustal structure of the western Mid-Atlantic Ridge flank, 25°25′–27°10′N and 0–29 m.y., *J. Geophys. Res.*, *102*(B5), 10,203–10,223, 1997.

Wolfe, C., G. M. Purdy, D. R. Toomey, and S. C. Solomon, Microearthquake characteristics and crustal velocity structure at 29°N of the Mid-Atlantic Ridge: The architecture of a slow-spreading segment, *J. Geophys. Res.*, *100*(B12), 24,449–24,472, 1995.

Yamada, T., K. Tamaki, H. Fujimoto, and T. Kanazawa, Microearthquakes characteristics at the Jourdanes segment: Seismic experiment at 64°E (SWIR). (abstract), paper presented at *InterRidge South West Indian Ridge Workshop*, InterRidge, Southampton, UK, 2002.